Earth and Space Science

RESEARCH ARTICLE
10.1029/2020EA001598

Model Age Derivation of Large Martian Impact Craters, Using Automatic Crater Counting Methods

A. Lagain[1], K. Servis[1,2], G. K. Benedix[1], C. Norman[1], S. Anderson[1], and P. A. Bland[1]

[1]Space Science and Technology Centre, School of Earth and Planetary Sciences, Curtin University, Perth, WA, Australia, [2]CSIRO - Pawsey Supercomputing Centre, Kensington, WA, Australia

Key Points:

- Automatic detection of small craters on ejecta blanket of 10 large Martian craters
- Identification of secondary craters through cluster analysis
- Model ages from our semi-automatic approach are similar from manual counts

Supporting Information:

- Supporting Information S1

Correspondence to:
A. Lagain,
anthony.lagain@curtin.edu.au

Citation:
Lagain, A., Servis, K., Benedix, G. K., Norman, C., Anderson, S., & Bland, P. A. (2021). Model age derivation of large Martian impact craters, using automatic crater counting methods. *Earth and Space Science*, *8*, e2020EA001598. https://doi.org/10.1029/2020EA001598

Received 11 DEC 2020
Accepted 26 DEC 2020

Author Contributions:
Conceptualization: A. Lagain
Writing – original draft: A. Lagain
Writing – review & editing: G. K. Benedix, S. Anderson, P. A. Bland

Abstract Determining when an impact crater formed is a complex and tedious task. However, this knowledge is crucial to understanding the geological history of planetary bodies and, more specifically, gives information on erosion rate measurements, meteorite ejection location, impact flux evolution and the loss of a magnetic field. The derivation of an individual crater's age is currently performed through manual counting. Because crater size scales as a power law, this method is limited to small (and/or young) surface areas and, in the case of the derivation of crater emplacement age, to a small set of impact craters. Here, we used a Crater Detection Algorithm, specifically retrained to detect small impact craters on large- and high-resolution imagery data set to solve this issue. We applied it to a global, 5 m/pixel resolution mosaic of Mars. Here, we test the use of this data set to date 10 large impact craters. We developed a cluster analysis tool in order to distinguish potential secondary crater clusters from the primary crater population. We then use this, filtered, crater population to date each large impact crater and evaluate our results against literature ages. We found that automated counting filtered through clustering analysis produced similar model ages to manual counts. This technique can now be expanded to much wider crater dating surveys, and by extension to any other kind of Martian surface. We anticipate that this new tool will considerably expand our knowledge of the geological events that have shaped the surface of Mars, their timing and duration.

Plain Language Summary The age of an impact crater on a planetary surface is a crucial constraint in determining erosion rate, the crater source of Martian meteorites and the impact cratering flux evolution. This kind of measurement requires the counting of many impact craters superposed on the ejecta blanket of the considered crater and is therefore limited by human capability. To solve this issue, we adapted an automatic tool to detect small impact craters on the surface of Mars. We also developed an automatic approach to identify and remove clusters of small likely secondary craters detected by our algorithm. We assume these clusters of craters are formed by fragments ejected by an impact that formed a primary crater and need to be removed from crater densities used for age derivations. We applied our technique on 10 large Martian impact craters whose the formation age has been derived using manual counts and reported in the literature. We compared these ages to ours, derived from automatic count and automatic secondary craters filtering. Our results are consistent and indistinguishable from an age inferred from a manual count. For the first time, we demonstrate that an automated approach can deliver geologically meaningful model ages.

1. Introduction

Impacts are the most common geologic process to effect planetary surfaces. Craters expose underlying crustal material, giving us a glimpse at the history of a surface, as well as provide us with "free" sample-return material from Mars, the Moon and asteroids, such as Vesta, in the form of meteorites (Kelley et al., 2003; McSween et al., 2013). They allow us to determine ages for the surfaces of other worlds. Their utility in helping us understand the geological evolution of other celestial bodies is undisputed (e.g., Costard, 2019; Fassett, 2016; Tanaka et al., 2014; Williams et al., 2014). The knowledge of a crater's formation age is therefore a crucial element, accessible through cratering density measurements on their ejecta blankets, their rims, or their floors. However, manual counting is a tedious task, only practical for small areas and/or very young surfaces, as it is greatly affected by human ability and submitted to biases in the recognition of impact structures and the measurement of their diameter (Robbins et al., 2014). In a previous paper (Benedix et al., 2020), we demonstrated our ability to automatically count kilometer-sized impact craters and derive

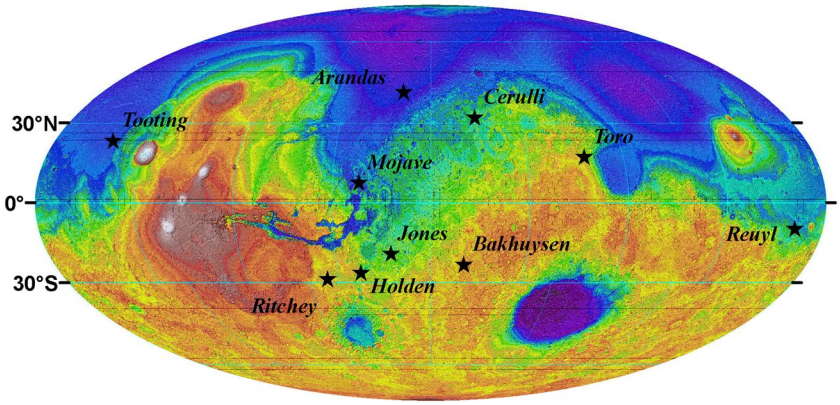

Figure 1. The locations of the craters considered in this study. Background image: MGS MOLA–MEX HRSC Blended DEM Global 200 m v2 (Fergason et al., 2018).

consistent surface ages using a Crater Detection Algorithm (CDA), specifically trained to detect impact structures on the surface of Mars using optical imagery. However, the dating of young or small geological units requires counting craters smaller than 1 km in diameter, which are naturally more numerous (e.g., Fassett, 2016; W. K. Hartmann, 2005; W. K. Hartmann & Neukum, 2001). Their distribution is also punctuated by secondary crater clusters produced from the ejecta of a larger impact event (e.g., Lagain et al., 2021; Robbins & Hynek, 2011, in press), thus creating a local anomaly of high cratering density which could potentially affect crater statistics (McEwen & Bierhaus, 2006; Wells, 2010; Williams et al., 2018). Secondary crater fields are considered separately in the development of chronology systems to derive model ages of the surface (e.g., W. K. Hartmann, 2005; W. K. Hartmann & Neukum, 2001; McEwen & Bierhaus, 2006; Robbins & Hynek, 2011; Shoemaker, 1965). In the past they have been manually identified and excluded thanks to a combination of their irregular shape and their relative position in a crater chain or crater cluster (McEwen et al., 2005; Roberts, 1964).

While irregularly shaped craters (highly elliptical, rim scalloped shape) are mostly missed by the previous version of the CDA (Benedix et al., 2020), circular secondary craters produced by high angle ejecta (Zhou et al., 2015) are detected. In this paper, we present the results of our CDA, retrained on high-resolution imagery datasets. Our aim is to detect smaller impact craters and derive surface ages, even in the context of geological units that are dominated by secondary craters. We selected and mapped the ejecta blanket of 10 large Martian impact craters, where manual counting and an age was performed and reported in the literature. We then applied our detection algorithm using the seam-corrected Context Camera (CTX) global mosaic from the MurrayLab (NASA/JPL/MSSS/The Murray Lab; Dickson et al., 2018). The spatial distribution of the detected population is then analyzed through a cluster analysis, presented in Section 2. We compare our results with model ages independently measured in Section 3 and then discuss our method and its implication in Section 4. We finally conclude and suggest future potential investigations in Section 5.

2. Methods

2.1. Crater Selection and Literature Model Ages

For this study, our focus is on named craters >20 km in diameter (482 craters according to the Robbins & Hynek, 2012 database). Impact craters considered here must exhibit a continuous ejecta layer (253 impact craters) and have published formation model ages. We also limit our focus to craters formed during the Amazonian or Hesperian period. We disregard Noachian impact craters, because their ejecta blankets are too degraded and they can only be dated by kilometric craters superposed onto their rims (Robbins et al., 2013). From a literature survey, we found 10 sites conforming to the above criteria; this corresponds to 4% of named craters >20 km with an ejecta blanket (Robbins & Hynek, 2012). Their locations are shown on the map in Figure 1. We briefly describe and recount model ages and chronology models reported in the literature in the Table 1 and Supplementary Text. Because we discuss different chronology systems, we review and provide some shorthand on the nomenclature used below, how Martian chronology systems have been

Earth and Space Science
10.1029/2020EA001598

Table 1
Name, Model Age and Statistical Information on the Model Age Reported in the Associated Reference for Each Crater Considered in This Study

Name	Diameter	Latitude	Longitude	Age		Diameter range	Chronology system	Fit	Reference	Comments
Arandas	24.8 km	42.4 N	15.0 W	390 Ma	+70 −70	354 m–1 km	W. K. Hartmann (2005)	P	Lagain et al. (2020)	Well-preserved ejecta layer morphology for this range of latitude, presence of field of secondary craters on the ejecta blanket
Bakhuysen	152.9 km	23.0S	15.8 E	3.5–3.8 Ga	–	1–8 km[a]	W. K. Hartmann (2005)	None	Tornabene et al. (2012)	Presence of crater-related pitted materials
				3.49 Ga	+0.07 −0.14	>1.25 km	W. K. Hartmann (2005)	C	Robbins et al. (2013)	
Cerulli	114.3 km	32.2 N	22.1 E	3.5 Ga	–	1–4 km[a]	W. K. Hartmann (2005)	None	Berman et al. (2011)	Derived from the raw value of the cratering density (N(1)), a method that lack of self-consistency between the two main chronology systems Robbins et al. (2013): Hartmann, (2005) and Neukum-Ivanov (2001)
Holden	152.7 km	26.0S	34.0 W	3.4 Ga	+0.11 −0.34	>1.2 km	W. K. Hartmann (2005)	C	Robbins et al. (2013)	Phyllosilicate-bearing strata post-dating its formation, lacustrine, fluvial and glacial morphologies
Jones	90.1 km	18.9S	19.8 W	3.6 Ga	+0.06 −0.10	1–3 km[a]	Neukum–Ivanov (2001)	C	Mangold et al. (2012)	Presence of fluvial valleys within the crater and numerous secondary chains ray and lobes around the crater
Mojave	58.0 km	7.5 N	33.0 W	8 Ma 3 Ma		50 m–250 m	Ivanov (2001)	?	Werner et al. (2014)	Thin ejecta layer, possible crater source of some Martian meteorites
Reuyl	78.7 km	9.6S	167.0 E	3.63 Ga	+0.04 −0.06	2–15 km[a]	Neukum–Ivanov (2001)	C	Vijayan et al. (2020)	Presence of alluvial fans and channel within the crater
Ritchey	77.2 km	28.5S	51.0 W	3.46 Ga	+0.11 −0.38	1–4 km[a]	Neukum–Ivanov (2001)	C	Sun and Miliken (2014)	Clay transport by fluvial processes within the crater, the counting area includes the inner part of the crater rim and only 1 crater radius from the rim over its ejecta, where most of the rim's erosion deposit lie
Tooting	27.9 km	23.2 N	152.2 W	0.4–1.7Ma	–	>54 m ?	W. K. Hartmann (2005)	?	Morris et al. (2010)	Possible crater source of some Martian meteorites
				2.9 Ma	–	10 m–60 m[a]	Neukum–Ivanov (2001)	?	Mouginis-Mark and Boyce (2012)	Small portion of the ejecta layer, close to the crater rim
				2–10 Ma	–	15 m–60 m[a]	W. K. Hartmann (2005)	None	W. K. Hartmann et al. (2010)	Small part of the crater interior and unspecified areas of the ejecta blanket
				0.8–4 Ma	–	–	Neukum–Ivanov (2001)	LS		
Toro	41.4 km	17.0 N	71.8 E	3.62 Ga	+0.07 −0.14	?	Ivanov (2001)	C	Fairen et al. (2010)	extensive aqueous activity within the crater

C, craterstats fitting technique, cumulative or incremental fit (Michael & Neukum, 2010); P, Poisson pdf fitting technique performed on CraterStats (Michael, 2016); LS, Least-square fitting technique.

[a]Graphic reading from the corresponding article.

developed and discuss one of the most important source of uncertainties in the context of our study: the role of the impacted material rheology in the size of impact craters.

Several systems have been developed linking the cratering density and crater sizes on planetary bodies with the age of the surface (see Fassett et al., 2016 for a recent review). These are mainly based on the extrapolation of the lunar chronology model, calibrated using the radiometric age of Apollo and Luna missions sample returns, to other terrestrial surfaces such as Mars (Hartmann, 1978; W. K. Hartmann and Neukum, 2001; Neukum & Ivanov, 1994;). These models are mostly dependent on the difference between the number of impactors hitting the surface between those bodies (i.e., their distance from the main source of impactors, the asteroid main belt) and the average impact velocity and gravity compared to the Moon. These parameters are summarized by a constant (known as the R factor) whose value is still the object of strong debate (W. K. Hartmann & Neukum, 2001; Ivanov, 2001; Ivanov et al., 2002; JeongAhn & Malhotra, 2015). Taking into account all of these variables the models tend to predict a smaller crater on Mars than on the Moon for the same impactor. Smaller craters are also predicted on bodies with atmospheres due to the effects that produce fragmentation and filtering (W. K. Hartmann, 2005; W. K. Hartmann & Daubar, 2017; Popova et al., 2003; Williams et al., 2014).

Crater counts on different material formed at the same time but exhibiting various rheology can potentially lead to a derivation of two different model ages because the physical properties of the surrounding ground play a major role in the size of the crater that forms on those surfaces (Kirchoff et al., 2015; Marchi et al., 2009; Van der Bogert et al., 2017; Williams et al., 2014). This source of bias is more important for craters ≤1 km in diameter, which are more sensitive to variations of the near-surface physical properties than larger impact structures (see section 2 in Lagain et al., 2020). Here we compare model ages derived from crater counts performed on the same geological unit, that is an ejecta blanket. Thus, this source of uncertainties does not influence the validity of our automatic method.

2.2. Ejecta Blanket Mapping, Data and Automatic Detection of Small Impact Craters Using CTX Imagery

Impact structures on Mars can be subject to one or more resurfacing events, for example due to intense aqueous activity or aeolian processes (see descriptions for Holden, Reuyl, Ritchey and Toro craters–Table 1 and Supplementary Text). Crater counting within the impact structure itself may be affected by this bias and, thus, the derived model age could correspond to the crater retention age (i.e., the age of the last large resurfacing episode), rather than the formation of the impact structure itself. Moreover, the area of the crater floor is also naturally smaller than the associated ejecta blanket that can potentially lead to a crater population that is too small to derive a reliable model age (Warner et al., 2015).

Continuous ejecta blankets, generated during the formation of the central large impact structure, constitute a better surface to retain small impact craters on Mars. For this study, we chose to define the inner border of the ejecta layer to 20% of the crater radius (as published by Robbins & Hynek, 2012) from the crater rim. This constraint minimizes the effect of resurfacing processes that might have affected the rims due to its inherent relief (sliding slope, aeolian erosion...). External borders of ejecta layers are restricted to the continuous portion of the blanket in order to limit the contamination of craters superposed on the surrounding ground and pre-dating the impact event. We mapped the ejecta blankets of our target craters using the THEMIS (Thermal Emission Imaging System) Day and Night Infra-Red mosaic (respectively v12 and v14, Edwards et al., 2011). The boundaries are illustrated in Figure 2 as thin blue lines.

The typical range of superposed crater diameters required to accurately date the impact craters described in Table 1 is 50 m–5 km. Reliable crater size depends on the effect of erosion/infilling of craters superposed to the dated surface. As larger craters are harder to obliterate, they are generally considered as more reliable to date planetary surface. Thus, counting areas larger than ~10,000 km^2 are recommended to derive model ages of a surface experiencing a moderate erosion rate (~25 nm/yr) (Palucis et al., 2020; Warner et al., 2015). Impact craters larger than 50 m in diameter are visible on the Mars Reconnaissance Orbiter Context Camera (CTX) images (5 m/px). CTX coverage of Mars is nearly global (~98%) and these images have been converted into a mosaic by the Murray Lab at Caltech (NASA/JPL/MSSS/TheMurrayLab, Dickson et al., 2018). The identification and removal of areas not covered by the global CTX mosaic from the final counting area (see

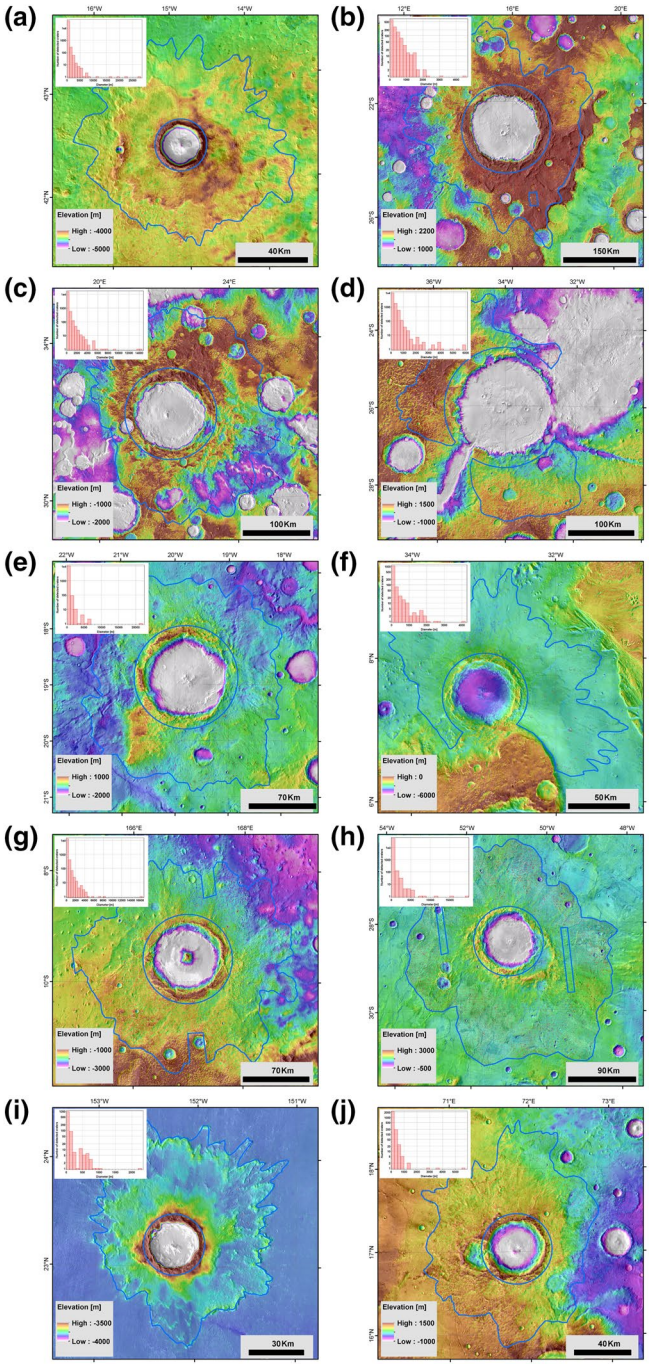

Figure 2. Ejecta blanket mapping of the 10 craters selected in this study (outlined in blue). All crater detections located on the blankets are visible on the online version of this article as red circles. The histogram shown at the top left of each sub-figure present their size-frequency distribution. (a) Arandas, (b) Bakhuysen, (c) Cerulli, (d) Holden, (e) Jones, (f) Mojave, (g) Reuyl, (h) Ritchey, (i) Tooting, (j) Toro. Background image: MGS MOLA–MEX HRSC Blended DEM Global 200 m v2 (Fergason et al., 2018) and THEMIS-IR Day Global Mosaic 100 m v12 (Edwards et al., 2011). The reader is referred to the web version of this manuscript for the visualization of the details of this figure (automatic detections and their size-frequency distribution).

strips orientated NW-SE on Figure 2h) constitutes the final step of the ejecta blanket mapping. These areas are shown on Figure 2 for all craters of the panel selected here.

The Crater Detection Algorithm (CDA) used to identify craters is described in detail by Benedix et al. (2020). This Convolutional Neural Network (CNN) was originally trained on the THEMIS Day IR mosaic where 1,762 craters from the Robbins and Hynek (2012) have been identified and manually cleaned to select the most identifiable impact craters. Applied to the THEMIS Day IR mosaic between 45 degrees of North and South, our algorithm produces a true positive detection rate of 86% for craters larger than 1 km in diameter (Benedix et al., 2020). However, the identification of smaller craters require higher resolution data set such as HiRISE (High-Resolution Imagery System Experiment) or CTX (Context Camera). When seen on these datasets, small craters exhibit a wide variety of morphologies, which imply a retraining of our model in order to obtain a satisfying detection rate. We retrained the CDA using HiRISE imagery datasets. For this, we used the HiRISE mosaic built by the Murray Lab (NASA/JPL/MSSS/TheMurrayLab, Dickson et al., 2018) covering a part of the Jezero crater (E77-5_N18_0) where 1,650 craters have been manually identified. A portion of this population of craters was selected to include the most confident impact features in the training data set, resulting in 1,624 craters over this entire image. This labeled data set was also augmented by applying the range of transformations described by Benedix et al. (2020) (rotate, shear, scale, and translate). We used this re-trained library and applied the CDA to the CTX data (Dickson et al., 2018) covering the ejecta blanket of the 10 selected craters, resulting in 129,799 detections larger than 70 m in diameter superposed on their blanket. All of these detections are visible on the online version of Figure 2 and a subset of crater detections over the Arandas ejecta blanket is also shown in Figures 3a and 3b.

2.3. Secondary Crater Identification by Cluster Analysis

Continuous ejecta blankets of large impact craters can retain a sufficient number of small impact craters to allow their dating through crater counting. Large impact craters are also known to exhibit a nonnegligible number of self-secondary craters (Caudill et al., 2018; Lagain et al., 2020; Zanetti et al., 2017). This makes them ideal surfaces to test the ability of our CDA to derive a consistent model age of their formation.

The identification and delineation of potential clusters of secondary impact craters is an essential key step during the process of surface age determination by crater counting. If they are not taken into account, it can potentially lead to a significant overestimation of the measured crater density (Zanetti et al., 2017), resulting in incorrect model ages. When crater counting is performed manually, an expert is able to identify and remove likely secondary craters belonging to a crater cluster and/or exhibiting an irregular morphology, which are common characteristics of secondary craters (McEwen & Bierhaus, 2006; Oberbeck & Morrison, 1974; Robbins & Hynek, 2011; Shoemaker, 1965). So long as the craters are circular our CDA is agnostic with respect to their origin, thus, these initial results incorporate the detection of numerous circular secondary craters as shown on Figure 3b. Although automated likely secondary crater recognition could not be implemented into our CDA

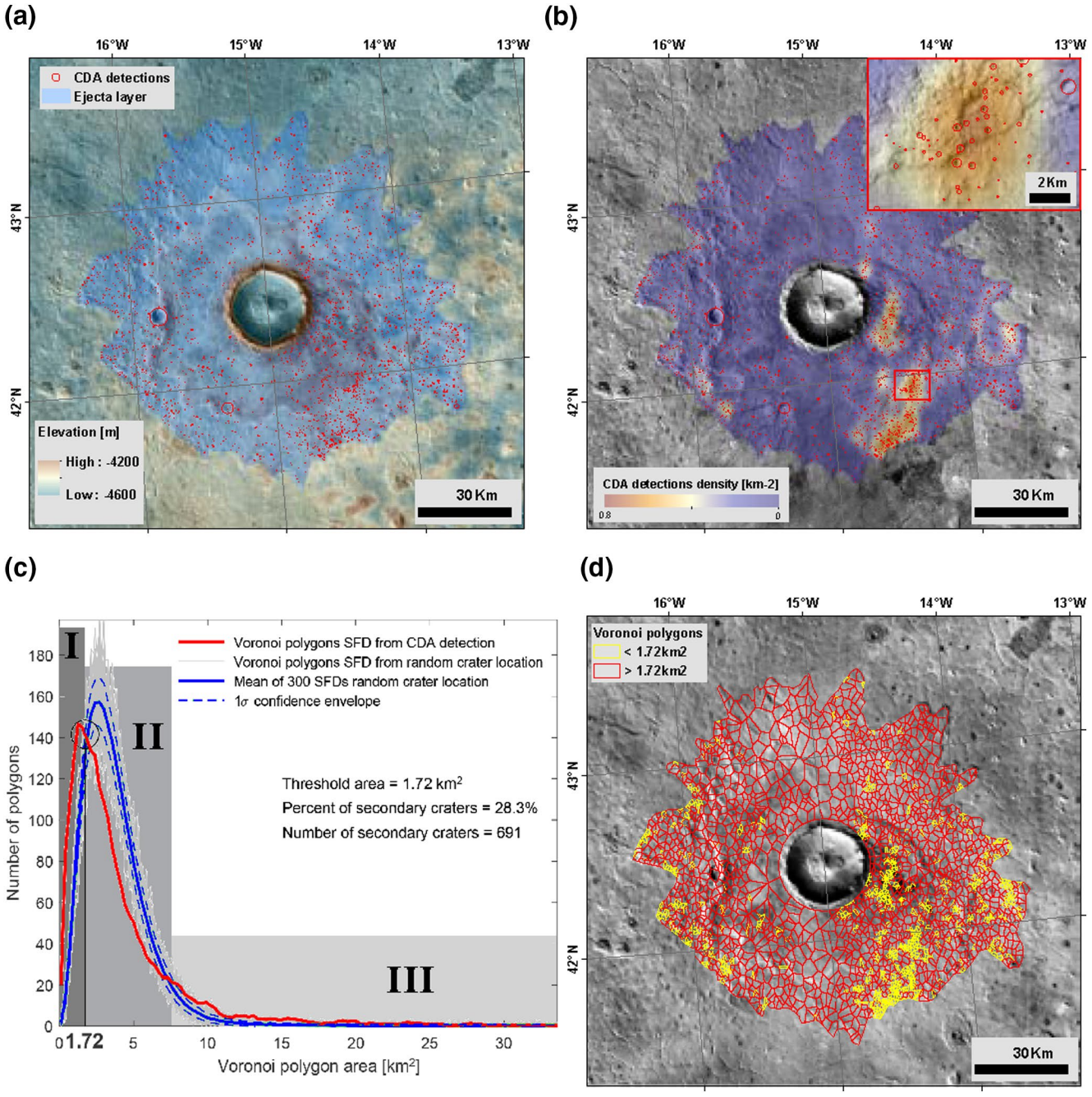

Figure 3. ASCI processing steps. (a) Arandas ejecta blanket and all CDA detections overlaid (2,443), background image: MGS MOLA–MEX HRSC Blended DEM Global 200 m v2 (Fergason et al., 2018) and THEMIS Day IR mosaic v12 (Edwards et al., 2011). (b) Cratering density map over the Arandas ejecta blanket. The top right corner of the figure shows a close-up of the most cratered area, dominated by likely secondary craters. All CDA detections are outlined in red. (c) Size-Frequency Distribution of VPs built from the CDA detection (in red) compared to 300 VPs SFD built from a population of craters containing the same number of craters than that detected by the CDA, randomly distributed over an area of the same size as the mapped ejecta blanket (in gray). Blue lines correspond to the mean of the 300 simulated VPs SFD and ±1σ confidence envelope. The intersection between the red curve and the simulated SFD at +1σ (black circle) corresponds to the threshold VP area −1.72 km^2-considered to identify crater clusters and thus distinguish likely primary and secondary craters over the Arandas ejecta blanket. (d) Voronoï polygons tessellation where VPs associated with primary and secondary craters are respectively outlined in red and yellow. The final counting area correspond to the whole ejecta blanket where VPs smaller than 1.72 km^2 have been removed. The crater population taken into account in the final model age derivation contains 1,752 detections: namely 72% of the whole detected crater population. ASCI, algorithm for the secondary crater identification; CFD, crater detection algorithm; SFD, size-frequency distribution; VP, Voronoï polygon.

directly, we have added a post-processing step that allows us to automatically reproduce a manual counting that avoids clusters of secondaries. We developed an Algorithm for the Secondary Crater Identification (ASCI) inspired from published approaches based on cluster analysis techniques (Andronov et al., 2016; Kreslavsky, 2007; Michael et al., 2012; Salih et al., 2017) and used as a post-process analysis of the crater population detected on each ejecta blanket. The main idea of ASCI is to identify potential secondary craters based on deviations from a calculated random distribution. Our approach is similar to that developed by Andronov et al. (2016) for the identification of protein clusters and allows the removal of likely secondary clusters as well as their associated area, based on deviations from a calculated random distribution.

In this section, we present in detail the different steps performed by the tool. We use the Arandas crater as an example to illustrate its efficiency as obvious crater clusters are found on its ejecta blanket (see cratering density map on Figure 3b), which are identical in scope to those detected through manual counts (Lagain et al., 2020).

Our approach uses a Voronoï polygon (VP) tessellation method (Voronoï, 1908). Each crater detected on a counting area is associated to a Voronoï polygon such as every point contained in the polygon is closer to the associated crater than to any other. VP tesselation is computed over a crater population detected on a counting area where the cratering density should be homogeneous–that is a surface formed at the same time–in this case the Arandas ejecta blanket (see Figure 3a).

We follow the ESRI's ArcMap procedure:

- All detected craters within the considered area are simplified as points and are then triangulated into a triangulated irregular network (TIN) that meets the Delaunay criterion, that is the requirement that the circumcircles of all triangles have empty interiors (Delaunay, 1924)
- The perpendicular bisectors for each triangle edge are generated, forming the edges of the Voronoï polygons. The location at which the bisectors intersect determines the locations of the Voronoï polygon vertices

The size-frequency distribution (SFD) of VPs is then calculated (red curve on Figure 3c). On the other side, 300 different impact crater populations containing the same number of craters than have been detected, are automatically generated with a randomized location. The associated VPs are computed for each of the 300 crater populations and their size-frequency distribution is calculated (gray curves on Figure 3c). Three hundred iterations are a good compromise between the statistically significance of the process and the computing time. The mean and the confidence envelope at $\pm$ 1σ of the simulated VPs SFD are computed (respectively the solid and dashed green curves on Figure 3c). We then define a cluster as a set of neighboring VPs with areas smaller than a given threshold. The intersection between the VPs SFD from detected (red curve on Figure 3c) and simulated at +1σ (upper blue dashed curve on Figure 3c) crater populations corresponds to the largest VP area in the clusters. This can be used as a threshold size (black circle on Figure 3c) to define the clusters. Detected craters found in smaller polygons are clustered (Andronov et al., 2016) and therefore, from a likely secondary origin (area I on Figure 3c and yellow polygons on Figure 3d). Those associated with a VP where the area is higher than the threshold value are considered random (areas II and III on Figure 3c and red polygons on Figure 3d). The corresponding craters are defined as primary. The crater count area is finally recalculated taking into account the removed VP (secondary) population (see Table S1 for all parameter values computed by the ASCI). If a manual checking of the secondary origin of each crater identified by ASCI is not feasible, a visual inspection has been performed in detail in the case of Arandas crater where secondaries identified using our procedure are shown on Figure 3b.

A comparison between the model age derived using the entire detected population and that obtained with the application of the ASCI is presented in the results section.

3. Results, Age Derivation, and Validation

The ASCI procedure has been applied to all the craters considered in this study (Table 1). Table S1 summarizes the potential secondary crater percentage along with entire detected population, the counting area and number of craters delineated as primaries or secondaries by the algorithm. To quantify the influence of the ASCI on the CSFD shape and derived model age, we compared the SFD of craters extracted from the ASCI

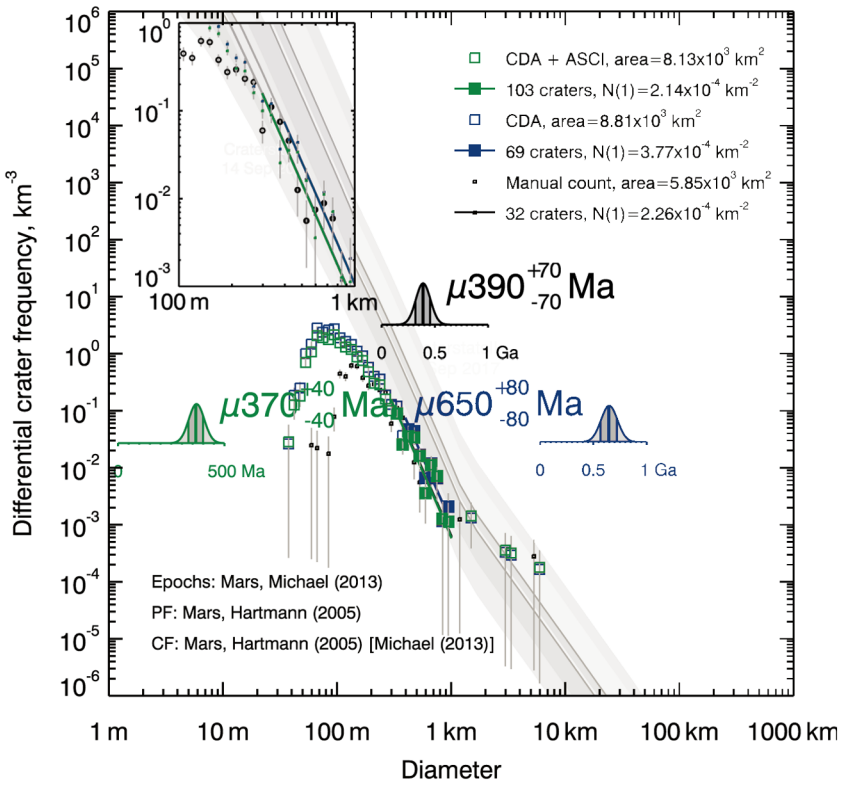

Figure 4. Comparison between the CSFD obtained from all detections over the Arandas ejecta blanket (in blue) and that obtained after the ASCI application (in green). In both cases, the Poisson fitting technique developed by Michael et al., 2016 was used to derive an age using the W. K. Hartmann (2005) production and chronology functions. The model age derived from the same technique by Lagain et al., 2020 is 390 ± 70 Ma (in black). The top left thumbnail is a close-up of all CSFDs between 100 m and 1 km. ASCI, algorithm for the secondary crater identification.

to all craters detected on each ejecta blanket. Each CSFD was loaded into CraterStats II (Michael & Neukum, 2010) and fitted with an isochron using the W. K. Hartmann (2005) CS (Chronology System). In this study, we decided to derive all model ages using the differential representation. The differential frequency at a given diameter D_x is $N(D_x) = n\,[D_{x1}, D_{x2}]/(D_{x2} - D_{x1})$ (Crater Analysis Group, 1979). The advantage of using this method instead of the usual cumulative plot, is that each point in the SFD is independent from the subsequent larger diameter bins. This allows easier recognition of the contribution of a resurfacing event or secondary craters (Chapman & Haefner, 1967; Fassett, 2016). Like other representations, the binning of the data can lead to biases when the CSFD is fitted with an isochron (Michael, 2016), a disadvantage solved by using the Poisson probability density function fitting technique (Michael, 2016). This solution allows a more precise match of the crater chronology model to the considered CSFD, whatever the chosen binning technique. We note that all isochrons have been fitted independently to each CSFD, which means that the diameter range used to fit an isochron with a CSFD can differ between the CSFD containing all craters and that containing only craters defined as primaries. Diameter ranges used to fit each CSFDs in our approach have been chosen independently for two reasons: (1) not all craters that have model ages reported in the literature have the associated crater diameter range used to derive it, (2) the counting area used here can differ from what has been used to derive the model ages reported in the literature, potentially implying a slightly different CSFD.

Figure 4 shows the results obtained for the Arandas ejecta blanket dating. The red CSFD corresponds to all craters detected on the ejecta blanket (blue area on Figures 3a and 3b) while the green CSFD corresponds only to primary craters on the modified counting area (Figures 3a and 3b) where all VPs smaller than 1.72 km^2 have been subtracted (yellow polygons on Figure 3d). While the CSFD corresponding to all craters detected on the ejecta blanket (2,243 > 70 m) has been fitted with an isochron using 69 craters ranging between 400 m and 1 km in diameter, the CSFD built from craters considered as primaries by the ASCI

(1,752 > 70 m) has been fitted with 103 craters ranging between 300 m and 1 km in diameter. In total, 28% of the entire detected population (691) has been identified as clustered and thus excluded from the final CFSD. With the inclusion of the ASCI procedure, the derived model age changes from 650 Ma-80+80 to 370 Ma-40+40. The latter age is identical, within error, to that reported by Lagain et al. (2020) where a manual counting (black CSFD on Figure 4), careful analysis of the crater distribution, and manual removal of secondaries, allowed the authors to derive an age of 390 Ma-70+70. In terms of cratering density for craters > 1 km in diameter inferred from each model age, N(1), the percentage of difference compared to the manual count is 5.4% using the CDA detection filtered by ASCI and 66.9% using the detection without using our cluster analysis.

Figure 5 shows the results obtained for all other craters following the same procedure as for the Arandas crater. Red curves correspond to the Poisson probability density function (PDF) of the age derived without the use of the ASCI (red isochrons on Figure S1) while green curves are the PDF of ages using the ASCI. Blue lines correspond to the impact model age reported in the literature, converted into the W. K. Hartmann (2005) CS (see Section 2.1). Wide blue intervals correspond to model age ranges given by authors of the considered study.

In 9 out of 10 cases, the model ages derived by applying the ASCI are lower, and closer to reported literature values using manual techniques than those derived from all craters detected on the ejecta blanket. Reuyl, Jones and Toro craters show overlap between the results, but the relative difference is insignificant (Figure 5).

Cerulli shows a ~100 Ma difference between the model age derived from all craters (3.60 Ga-0.018+0.016) versus that from primaries (3.49 Ga-0.023+0.020) only. The latter is very close to the model age reported by Berman et al. (2011). Bakhuysen crater is the only crater in this study exhibiting a discrepancy between the model age inferred through our automatic process and the model age derived from a manual count. While Robbins et al. (2013) reports an age of 3.49 Ga-0.14+0.07. we estimate the formation age of this impact event to 3.56 Ga-0.012+0.011 So even in this case the auto-derived age from the CDA and ASCI filtering is identical to the manual count analysis, within the Robbins' model age uncertainties. Model ages derived for Holden and Ritchey craters using automatic counts filtered through the ASCI are closer to the model ages inferred from manual counts and both intersect the ages reported in the literature when considering uncertainties. Tooting and Mojave, the youngest craters both in this study and of this size range on Mars, exhibit a significant reduction in model age (by a factor of ~2) when the ASCI is applied over the entire detection population of craters superposed on their ejecta blanket. In the case of Tooting crater, both model ages reported in the literature have been derived from manual count performed on small portions of the crater interior using HiRISE images (W. K. Hartmann et al., 2010 reported a model age where an unspecified portion of the counted population is located on the ejecta blanket). When Mouginis-Mark and Boyce (2012) report a ~3 Ma model age, Hartmann (2010) gave a model age range between 2 and 10 Ma thus intersecting model age reported by Mouginis-Mark and Boyce (2012) and that measured in our study, that is 7.7 ± 3 Ma. Finally, the model age of Mojave crater reported by Werner et al. (2014) is ~2.1 Ma using the W. K. Hartmann (2005) CS while the model age we report using automatic count filtered with the ASCI is 10.1 Ma-0.59+0.49. We discuss the reason for this discrepancy below.

4. Discussion

The relatively minor difference observed between the ages derived from automatic versus manual counting (Figures 4 and 5) suggests that the technique we use here is valid for the set of Martian craters presented in this paper. The results are indistinguishable—within error—from the age reported in the literature when the distribution of the detected crater population is analyzed through ASCI. Furthermore, the differences, with or without using ASCI, for the three oldest impact craters dated at the transition between the Hesperian and Noachian epoch (Toro, Jones, and Reuyl) is insignificant (Figure 5). For these craters, the CSFD was fitted using craters larger than 1 km in diameter. The influence of circular secondaries at this diameter range is particularly low as a typical secondary CSFD is steeper than that of primaries. Therefore, using the ASCI does not appear to influence the portion of the CSFD dominated by large impact craters. The ASCI is most applicable to smaller craters, as an automated post-processing supplement to the CDA.

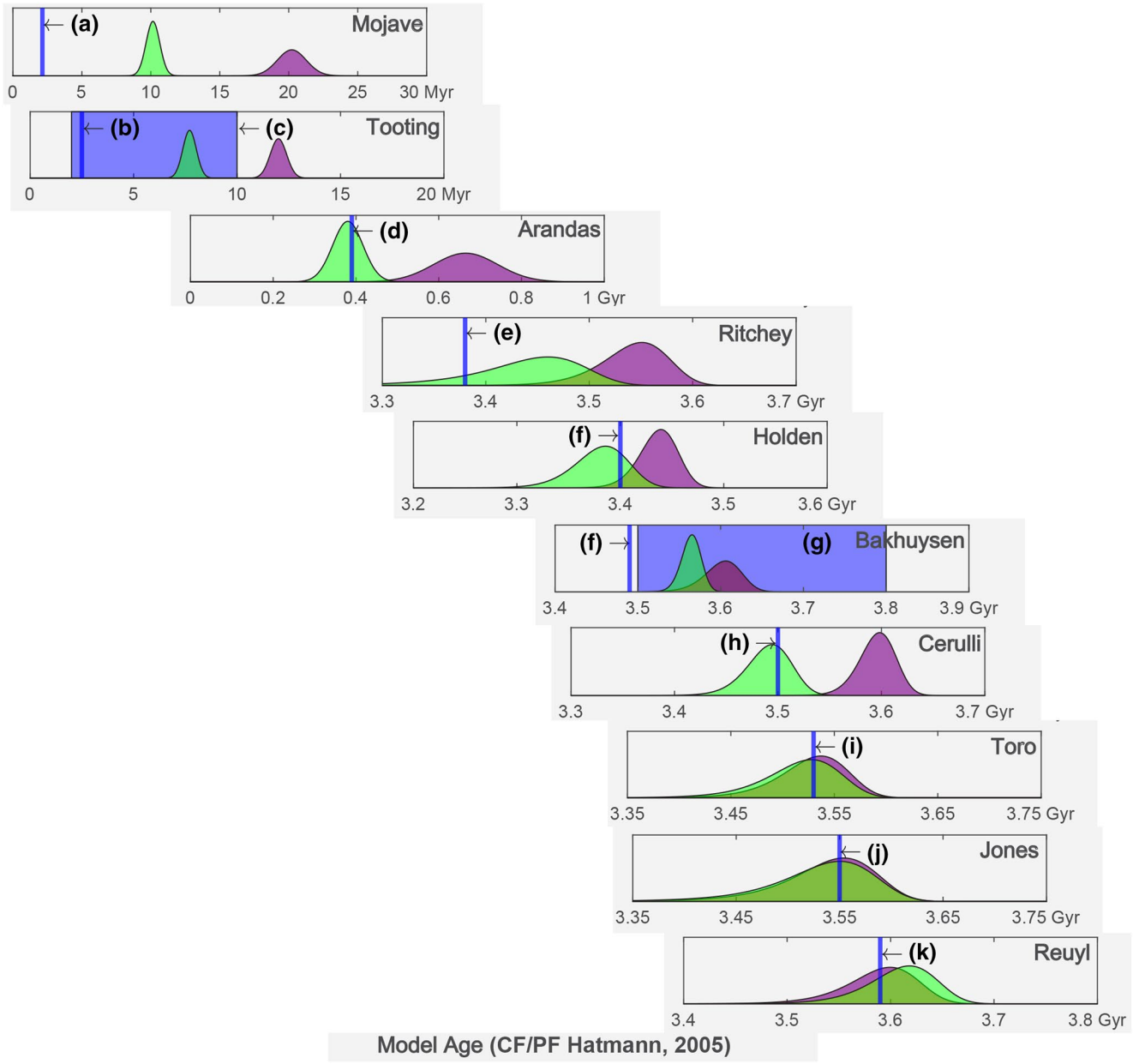

Figure 5. Graphical representation of model ages derived for each crater with and without using the ASCI, corresponding respectively to the green and the puple curve. The blue bar corresponds to the age reported in the literature and derived from isochron fitting from manual count: (a) Werner et al., 2014; (b) Mouginis-Mark et al., 2012; (d) Lagain et al., 2020; (e) Sun and Miliken, 2014; (f) Robbins et al., 2013; (g) Tornabene et al., 2012; (h) Berman et al., 2011; (i) Fairen et al., 2010; (j) Mangold et al., 2012; (k) Vijayan et al., 2020. Large blue bars correspond to an interval of ages reported in the literature by additional authors: (c) W. K. Hartmann et al., 2010 based on isochron fitting; (g) Tornabene et al., 2012 report a modeled crater-retention age consistent with late Noachian or Noachian–Hesperian time, roughly spanning a period from 3.5 and 3.8 Ga. ASCI, algorithm for the secondary crater identification.

The application of the ASCI cluster analysis has the effect of decreasing the crater density of small craters (~100 m) because crater clusters are mainly dominated by small structures (see Figure S1). The minimum crater diameter used to fit the CSFD obtained using the ASCI with an isochron is either equal to or smaller than the minimum crater diameter used in the fitting of the isochrons without the cluster analysis (see Table S1). This allows the inclusion of more craters in the portion of the CSFD fitted with an isochron, decreasing the uncertainties on the derived model age.

Among the 10 craters considered in this study, Mojave crater is the only one where the CDA/ASCI-derived age diverges significantly from that derived from a manual count (Figure 5). It is also the only impact struc-

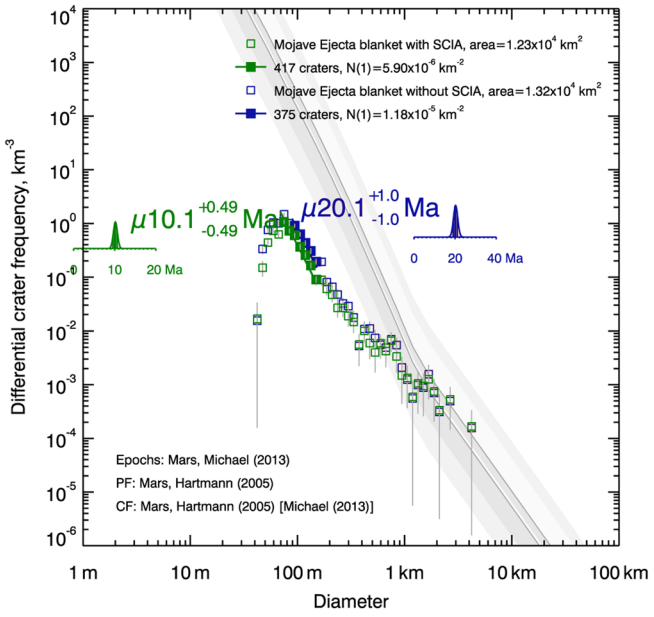

Figure 6. Formation model age of Mojave crater obtained from all detections (in blue) and after the ASCI application (in green). The branch of the CSFD corresponding to craters larger than 200 m likely represent the cratering record of the impacted material covered by the ejecta blanket. ASCI, algorithm for the secondary crater identification.

ture exhibiting such thin radial ejecta blanket. Its corresponding CSFD, as well as that of Tooting, exhibits two branches where an isochron can be fitted (see supplementary figure and Figure 6). The portion associated with craters larger than ~1 km in diameter corresponds to impact craters superposed on the surrounding ground and overlapped by the ejecta blanket We therefore suggest the possibility of having overestimated Mojave's model formation age due to the inclusion of some craters underneath the thin ejecta blanket, and instead may be representative of the formation age of the surrounding/underlying terrain. Overlapped crater recognition is made particularly difficult when an ejecta blanket acts only as a thin veneer over the surrounding ground. However, this model age is relatively close, and therefore consistent, with manually derived model age (Figure 5) regarding the large variability of young model ages (Williams et al., 2017), which is induced by several factors including differences in identification and diameter estimation by different manual counters (Robbins et al., 2014).

Manual crater counts of craters superposed on the ejecta blanket of large impact craters considered in this study do not specify the number of secondary craters found and excluded from the counting. This makes impossible any independent comparison between results obtained from our automatic approach and those from manual counts. However, as the secondary CSFD is much steeper than that of primary craters, if ASCI significantly under- or over-estimated the number of secondaries, the correspondence between published ages and that we derive here from automatic counting would not be observed. We therefore conclude that is reasonable to state that ASCI estimates as best as a human do, the number of secondaries over a counting area.

The use of ASCI alongside the automated crater detections provides a reproducible and consistent way to identify clusters of craters. These clusters are most likely to be secondary craters (Figures 3c and 3d), but there will also be some small primary craters within these populations. There could even be clusters of craters that are primary due to meteorite breakup in the atmosphere (W. K. Hartmann & Daubar, 2017). However, even manually distinguishing small primary craters among a cluster of secondary craters is particularly difficult, even impossible. The automated analysis using the Voronoï tessellation technique at least allows the effect to be quantified in a consistent and reproducible way to extract a CSFD representative of the crater age.

The exclusion of the VPs that do not meet the randomness criteria defined in Section 2 in the calculation of the final counting area allows us to counterbalance the loss of primaries within the clusters in the final set of craters. It is also expected that applying ASCI over an area where the crater clusters dominate the entire crater population, within a crater cluster, on an area too small, or exhibiting a too low number of impact craters would lead undoubtedly to an obvious secondary craters identification bias and/or introducing a nonnegligible effect of crater degradation into the analysis of the CSFD (Fassett et al., 2020). We therefore recommend the users to apply this method over an area that has been investigated before to make sure that the mapped area fit the requirements usually admitted to derive an age (see Williams, 2018 for a complete list of potential issues). It is important to note that this method is not a black box, but serves to provide guidance for identifying potential secondary craters. This method is faster than manual counting so that the user can use it to pinpoint the areas on the surface to investigate in depth.

5. Conclusions and Perspectives

The automatic crater count using our CDA coupled with the use of a cluster analysis algorithm to identify potential contamination by secondary crater clusters (ASCI) is a powerful tool for generating reliable crater SFDs for surfaces of Mars (or any other planetary surfaces using appropriate training datasets) even in a

context of likely secondary crater contamination. Model ages estimated using this technique are consistent with those reported in the literature obtained from manual counting. The combination of both tools provides an automated route for determining the emplacement age of many impact craters. When combined with careful analysis and cautious characterization of the influence of degradation processes, this method can be extensively used to investigate potential temporal fluctuation in the size frequency distribution of impact craters, and, when applied to other geological structures, to reconstruct the geological history of a portion of the Martian surface at a regional scale as well as the spatial and temporal evolution of the volatile-rich subsurface layer through the systematic dating of large layered ejecta craters. This will be the focus of future work.

Software

ASCI is available for others to use as a software extension for Environmental Systems Research Institute's (ESRI's) ArcMap (ArcGIS) at the following address: https://github.com/curtin-crater-detection/secondary-crater-removal.

Data Availability Statement

The data that support the findings of this study are openly available at http://doi.org/10.5281/zenodo.4383457.

Acknowledgments
The authors acknowledge Peter Fox, Caleb Fassett, Michelle Kirchoff and an anonymous reviewer for thorough and helpful reviews and comments that improved this manuscript. This work was supported by the resources provided by the Pawsey Supercomputing Center with funding from the Australian Government, Curtin University, and the Government of Western Australia. This research is funded by the Australia Research Council (DP170102972 and FT170100024) and Curtin University. We are grateful the Murray Lab for the building and the release of the HiRISE mosaics covering the Jezero crater area used to retrain our Crater Detection Algorithm, as well as the CTX global mosaic, making this work possible. We thank the Curtin Hub for Immersive Visualization and eResearch (HIVE) for their help in the visualization of our crater detection having allowed the improvement of our algorithm as well as their work on the MOLA/HRSC mosaic presented in Figure 1.

References

Andronov, L., Orlv, I., Lutz, Y., Vonesch, J.-L., & Klaholz, B. P. (2016). ClusterViSu, a method for clustering of protein complexes by Voronoï tessellation in super-resolution microscopy. *Nature, Scientific Reports*, *6*(24084), 2045–2322.

Benedix, G. K., Lagain, A., Chai, K., Meka, S., Anderson, S., Norman, C., et al. (2020). Deriving surface ages on Mars using automated crater counting. *Earth and Space Science*, *7*, e2019EA001005. https://doi.org/10.1029/2019EA001005

Berman, D. C., Crown, D. A., & Emily, C. S. (2011). Determining erosional/depositional history of Deuteronilus Mensae, Mars using categorized crater size-frequency distributions. *42nd Lunar and Planetary Science Conference*, The Woodlands, Texas. Abstract #1435.

Caudill, C. M., Osinski, G. R., & Tornabene, L. L. (2018). Ejecta deposits of Bakhuysen crater, Mars. *Icarus*, *314*, 175–194.

Chapman, C. R., & Haefner, R. R. (1967). A critique of methods for analysis of the diameter-frequency relation for craters with special application to the Moon. *Journal of Geophysical Research*, *72*, 549–557.

Costard, F., Séjourné, A., Lagain, A., Ormö, J., Rodriguez, J. A. P., et al. (2019). The Lomonosov crater impact event: A possible mega-tsunami source on Mars. *Journal of Geophysical Research: Planets*, *124*(7), 1840–1851. https://doi.org/10.1029/2019JE006008

Delaunay, B. (1924). On the empty sphere. In *Proceedings in the International Congress of Mathematicians*, 695–700.

Dickson, J. L., Kerber, L. A., Fassett, C. I., & Ehlmann, B. L. (2019). A global, blended CTX mosaic of Mars with vectorized seam mapping. A new mosaicking pipeline using principles of non-destructive image editing. In *49th Lunar and Planetary Science Conference*, Woodlands, TX.

Edwards, C. S., Nowicki, K. J., Christensen, P. R., Hill, J., Gorelick, N., & Murray, K. (2011). Mosaicking of global planetary image datasets: 1. Techniques and data processing for Thermal Emission Imaging System (THEMIS) multi-spectral data. *Journal of Geophysical Research*, *116*, E10008. https://doi.org/10.1029/2010JE003755

Fairén, A. G., Chevrier, V., Abramov, O., Marzo, G. A., Gavin, P., Davila, A. F., et al. (2011), Noachian and more recent phyllosilicates in impact craters on Mars. *Proceedings of the National Academy of Sciences of the United States of America 107*, 12095–12100. https://doi.org/10.1073/pnas.1002889107. pmid: 20616087

Fassett, C. I. (2016). Analysis of impact crater populations and the geochronology of planetary surfaces in the inner solar system. *Journal of Geophysical Research: Planets*, *121*, E10. https://doi.org/10.1002/2016JE005094

Fassett, C. I., Watters, A., Hundal, C. B., & Zanetti, M. (2020). Spatial variation in erosion rates in Mars equatorial regions inferred from ejecta retention of 1–3 Km diameter craters. *51st Lunar and Planetary Science Conference.* Abstract #1586.

Fergason, R. L., Hare, T. M., & Laura, J. (2018). *HRSC and MOLA blended digital elevation model at 200m v2. Astrogeology PDS annex.*. U.S. Geological Survey. http://bit.ly/HRSC_MOLA_Blend_v0

Hartmann, W. K. (1978). Martian cratering V: Toward an empirical martian chronology, and its implications. *Geophysical Research Letters*, *5*, 450–452.

Hartmann, W. K. (2005). Martian cratering 8: Isochron refinement and the chronology of Mars. *Icarus*, *174*, 294–320. https://doi.org/10.1016/j.icarus.2004.11.023

Hartmann, W. K., & Daubar, I. J. (2017). Martian cratering 11. Utilizing decameter scale crater populations to study Martian history. *Meteoritics and Planetary Science*, *52*, 3. https://doi.org/10.1111/maps.12807

Hartmann, W. K., & Neukum, G. (2001). Cratering chronology and evolution of Mars. In R. Kallenbach, J. Geiss, & W. K. Hartmann (Eds.), *Chronology and evolution of Mars* (pp. 165–194). Bern: International Space Science Institute.

Hartmann, W. K., Quantin, C., Werner, S. C., & Popova, O. (2010). Do young martian ray craters have ages consistent with the crater count system?. *Icarus*, *208*, 621–635. https://doi.org/10.1016/j.icarus.2010.03.030

Ivanov, B. A. (2001). Mars Moon cratering rate ratio estimates. *Chronology and Evolution of Mars*, *96*, 87–104.

Ivanov, B. A., Neukum, G., Bottke, W. F., & Hartmann, W. K. (2002). The comparison of size-frequency distributions of impact craters and asteroids and the planetary cratering rate. In W. F. Bottke et al. (Eds.), *Asteroids III* (pp. 90–101). Tucson: University of Arizona.

JeongAhn, Y., & Malhotra, R. (2015). The current impact flux on Mars and its seasonal variation. *Icarus*, *262*, 140–153.
Kelley, M. S., Vilas, F., Gaffey, M. J., & Abell, P. A. (2003). Quantified mineralogical evidence for a common origin of 1929 Kollaa with 4 Vesta and the HED meteorites. *Icarus*, *165*, 215–218.
Kirchoff, M. R., Marchi, S., & Wünnemann, K. (2015). The effects of terrain properties on determining crater model ages of lunar surfaces. In 46th Lunar and Planetary Science Conference #2121.
Kreslavsky, M. A. (2007). Statistical characterization of spatial distribution of impact craters: Implications to present-day cratering rate on Mars. *LPI Contribution*, *1353*, 3325–3328.
Lagain, A., Bouley, S., Baratoux, D., Costard, F., & Wieczorek, M. (2020). Impact cratering rate consistency test from ages of layered ejecta on Mars. *Planetary and Space Science*, *180*, 104755. https://doi.org/10.1016/j.pss.2019.104755
Mangold, N., Adeli, S., Ansan, V., & Langlais, B. (2012). A chronology of early Mars climatic evolution from impact crater degradation. *Journal of Geophysical Research*, *117*, E4. https://doi.org/10.1029/2011JE004005
Marchi, S., Mottola, S., Cremonese, G., Massironi, M., & Martellato, E. (2009). A new chronology for the moon and mercury. *The Astronomical Journal*, *137*(2009), 4936–4948. https://doi.org/10.1088/0004-6256/137/6/4936
McEwen, A. S., & Bierhaus, E. B. (2006). The importance of secondary cratering to age constraints on planetary surface. *Annual Review of Earth and Planetary Sciences*, *34*(1), 535–567. https://doi.org/10.1146/annurev.earth.34.031405.125018
McEwen, A. S., Preblich, B. S., Turtle, E. P., Artemieva, N. A., Golombek, M. P., Hurst, M., et al. (2005). The rayed crater Zunil and interpretations of small impact craters on Mars. *Icarus*, *176*, 351–381. https://doi.org/10.1016/j.icarus.2005.02.009
McSween, H. Y., Jr, Binzel, R. P., De Sanctis, M. C., Ammannito, E., Prettyman, T. H., Beck, A. W., et al. (2013). Dawn: The Vesta–HED connection; and the geologic context for eucrites, diogenites, and howardites. *Meteoritics and Planetary Science*, *48*, 2090–2104.
Michael, G. G., Kneissl, T., & Neesemann, A. (2016). Planetary surface dating from crater size-frequency distribution measurements: Poisson timing analysis. *Icarus*, *277*, 279–285.
Michael, G. G., & Neukum, G. (2010). Planetary surface dating from crater size frequency distribution measurements: Partial resurfacing events and statistical age uncertainty. *Earth and Planetary Science Letters*, *294*, 223–229.
Michael, G. G., Platz, T., Kneissl, T., & Neesemann, A. (2012). Planetary surface dating from crater size frequency distribution measurements: Spatial randomness and clustering. *Icarus*, *218*, 169–177.
Mouginis-Mark, P. J., & Boyce, J. M. (2012). Tooting crater: Geology and geomorphology of the archetype large, fresh, impact crater on Mars. *Chemie der Erde–Geochemistry*, *72*(1), 1–23. https://doi.org/10.1016/j.chemer.2011.12.001
Neukum, G., & Ivanov, B. A. (1994). Crater size distributions and impact probabilities on Earth from Lunar, Terrestrial-Planet, and asteroid cratering data. In T. Gehrels (Ed.), *Hazards due to comets and asteroids* (pp. 359–416). Tucson: University of Arizona Press.
Oberbeck, V. R., & Morrison, R. H. (1974). Laboratory simulation of the herringbone pattern associated with lunar secondary crater chains. *The Moon*, *9*, 415–455. http://dx.doi.org/10.1007/BF00562581
Palucis, M. C., Jasper, J., Garczynski, B., & Dietrich, W. E. (2020). quantitative assessment of uncertainties in modeled crater retention ages on Mars. *Icarus*, *314*, 113623. https://doi.org/10.1016/j.icarus.2020.113623
Popova, O., Nemtchinov, I., & Hartman, W. K. (2003). Bolides in the present and past martian atmosphere and effects on cratering processes. *Meteoritics & Planetary Sciences*, *38*, 905–925.
Robbins, S. J., Antonenko, I., Kirchoff, M. R., Chapman, C. R., Fassett, C. I., Herrick, R. R., et al. (2014). The variability of crater identification among expert and community crater analysts. *Icarus*, *234*, 109–131. https://doi.org/10.1016/j.icarus.2014.02.022
Robbins, S. J., & Hynek, B. M. (2011). Secondary crater fields from 24 large primary craters on Mars: Insights into nearby secondary crater production. *Journal of Geophysical Research*, *116*, E10003. http://dx.doi.org/10.1029/2011JE003820
Robbins, S. J., & Hynek, B. M. (2012). A new global database of Mars impact craters ≥1 km: 1. Database creation, properties, and parameters. *Journal of Geophysical Research*, *117*, E05004. https://doi.org/10.1029/2011JE003966
Robbins, S. J., Hynek, B. M., Lillis, R. J., & Bottke, W. F. (2013). Large impact crater histories of Mars: The effect of different model crater age techniques. *Icarus*, *225*, 173–184. http://dx.doi.org/10.1016/j.icarus.2013.03.019
Roberts, W. A. (1964). Secondary craters. *Icarus*, *3*, 348–364. https://doi.org/10.1016/0019-1035(64)90045-4
Salih, A. L., Lompart, A., Grumpe, A., Wöhler, C., & Hiesinger, H. (2017). AUTOMATIC DETECTION OF SECONDARY CRATERS AND MAPPING OF PLANETARY SURFACE AGE BASED ON LUNAR ORBITAL IMAGES. *ISPRS - International Archives of the Photogrammetry, Remote Sensing and Spatial Information Sciences*, *XLII-3/W1*, 125–132. https://doi.org/10.5194/isprs-archives-xlii-3-w1-125-2017
Shoemaker, E. M. (1965). Preliminary analysis of the fine structure of the lunar surface in Mare Cognitum. In W. N. Heiss, D. R. Menzel, & J. A. O'Keefe (Eds.), *The nature of the lunar surface* (pp. 23–77). Baltimore, MD: Johns Hopkins University Press.
Sun, V. Z., & Milliken, R. E. (2014). The geology and mineralogy of Ritchey crater, Mars: Evidence for post-Noachian clay formation. *Journal of Geophysical Research: Planets*, *119*, 4. https://doi.org/10.1002/2013JE004602
Tanaka, K. L., Skinner, J. A., Jr., Dohm, J. M., Irwin, E. J., III, Kolb, E. J., Fortezzo, C. M., et al. (2014). Geologic map of Mars (Vol. 3292). U.S. Geological Survey Scientific Investigations Map. http://dx.doi.org/10.3133/sim3292
Tornabene, L. L., Osinski, G. R., McEwen, A. S., Boyce, J. M., Bray, V. J., et al. (2012). Widespread crater-related pitted materials on Mars: Further evidence for the role of target volatiles during the impact process. *Icarus*, *220*, 348–368. https://doi.org/10.1016/j.icarus.2012.05.022
Van der Bogert, C. H., Hiesinger, H., Dundas, C. M., Kruger, T., McEwen, A. S., Zanetti, M., & Robinson, M. S. (2017). Origin of discrepancies between crater size-frequency distributions of coeval lunar geologic units via target property contrasts. *Icarus*, *298*, 49–63. https://doi.org/10.1016/j.icarus.2016.11.040
Vijayan, S., Sinha, R. S., Harish, & Anilkumar, R. (2020). Evidence for multiple superposed fluvial deposits within Reuyl Crater, Mars. *Journal of Geophysical Research: Planets*, *125*, 3. https://doi.org/10.1029/2019JE006136
Voronoï, G., (1908) Nouvelles applications des paramètres continus à la théorie des formes quadratiques. Premier mémoire. Sur quelques propriétés des formes quadratiques positives parfaites. *Journal für die Reine und Angewandte Mathematik*, *1908*, 198–287.
Warner, N. H., Gupta, S., Calef, F., Grindrod, P., Boll, N., & Goddard, K. (2015). Minimum effective area for high resolution crater counting of martian terrains. *Icarus*, *245*, 198–240. https://doi.org/10.1016/j.icarus.2014.09.024
Wells, K. S., Campbell, D. B., Campbell, B. A., & Carter, L. M. (2010). Detection of small lunar secondary craters in circular polarization ratio radar images. *Journal of Geophysical Research*, *115*, E06008. https://doi.org/10.1029/2009JE003491
Werner, S. C., Ody, A., & Poulet, F. (2014). The source crater of Martian Shergottite meteorites. *Science*, *343*(6177), 1343–1346. https://doi.org/10.1126/science.1247282
Williams, J.-P., Pathare, A. V., & Aharonson, O. (2014). The production of small primary craters on Mars and the Moon. *Icarus*, *235*, 23–36. https://doi.org/10.1016/j.icarus.2014.03.011

Williams, J.-P., van der Bogert, C. H., Pathare, A. V., Michael, G. G., Kirchoff, M. R., & Hiesinger, H. (2017). Dating very young planetary surfaces from crater statistics: A review of issues and challenges. *Meteoritics and Planetary Science*, *53*(4), 554–582. https://doi.org/10.1111/maps.12924

Zanetti, M., Stadermann, A., Jolliff, B., Hiesinger, H., van der Bogert, C. H., & Plescia, J. (2017). Evidence for self-secondary cratering of Copernican-age continuous ejecta deposits on the Moon. *Icarus*, *298*, 64–77.

Zhou, S., Xiao, Z., & Zeng, Z. (2015). Impact craters with circular and isolated secondary craters on the continuous secondaries facies on the Moon. *Journal of Earth Sciences*, *26*, 740–745.